Supplementary Information for *A time-direction field linking GR redshift, decoherence, and horizon thermality*

Behnam Dehghani
Intelitive Research Lab, Amadora, Lisbon, Portugal
Email: bd@intelitive.com Tel: +351-932-297-030

Contents

Conventions

We set $c = \hbar = k_B = 1$ unless explicitly stated. Metric signature $(-,+,+,+)$. "Observed" frequencies/temperatures are with respect to the laboratory (or asymptotic) time coordinate. All vectors in the internal time plane are dimensionless. Boldface denotes spatial tensors when needed.

1 Axioms, definitions, and immediate consequences (Note S1)

Axiom 1 (Unit-time vector (constancy))**.** *There exists a two-component time vector* $\vec{T} = (T_r, T_i) \in \mathbb{R}^2_{\geq 0}$ *with invariant norm*

$$\left\|\vec{T}\right\| = 1 \quad \Longleftrightarrow \quad T_r^2 + T_i^2 = 1. \tag{1}$$

Axiom 2 (Pulsed realization)**.** *Time unfolds as a sequence of discrete pulses* $\{\vec{T}^{(n)}\}_{n\in\mathbb{Z}}$ *with* $\left\|\vec{T}^{(n)}\right\| = 1$*. Between pulses, the vector vanishes; at each pulse it reappears with a (possibly) different direction.*

Axiom 3 (No pure axis (irreducible blend))**.** *Let* $\vartheta^{(n)}$ *be the polar angle of* $\vec{T}^{(n)}$*, so* $T_r^{(n)} = \cos\vartheta^{(n)}$*,* $T_i^{(n)} = \sin\vartheta^{(n)}$*. For all pulses*

$$0 < \vartheta^{(n)} < \tfrac{\pi}{2}. \tag{2}$$

Thus neither component ever vanishes; there is no purely unitary nor purely dissipative pulse.

Definition 1 (Coupling to observables)**.** *Experimental (instrumental) observables couple predominantly to* T_r*; phenomenological/entropic observables couple to* T_i*. The perceived flow of time tracks the sequence* $\{T_i^{(n)}\}$*; clock readings track* $\{T_r^{(n)}\}$*.*

Remark 1 (State dependence)**.** *The direction* $\vartheta(x)$ *may depend on contextual parameters (curvature, acceleration, entropy rate, environment), while the norm* (1) *is invariant.*

Parametrization. Write

$$\vec{T} = (\cos\vartheta, \sin\vartheta), \qquad 0 < \vartheta < \tfrac{\pi}{2}. \tag{3}$$

Define the lapse renormalization

$$A(\vartheta) = \sqrt{\cos^2\vartheta + \kappa\,\sin^2\vartheta}, \qquad \kappa \geq 0, \tag{4}$$

and its log-derivative

$$g_\vartheta(\vartheta) := \partial_\vartheta \ln A(\vartheta) = \frac{(\kappa-1)\sin\vartheta\cos\vartheta}{\cos^2\vartheta + \kappa\sin^2\vartheta}. \tag{5}$$

Useful identities:

$$\partial_\vartheta \ln T_r = -\tan\vartheta, \qquad \partial_\vartheta \ln T_i = \cot\vartheta. \tag{6}$$

Consequences. Axiom 3 implies $T_r, T_i \in (0,1)$, hence (i) no exactly unitary pulse; (ii) no exactly frozen dissipation. This yields the *intrinsic decoherence floor* once open-system dynamics are written in GKSL form (Sec. 3).

2 Redshift renormalization: derivation and weak-field bounds (Note S2)

2.1 General static spacetimes

For a static metric with Killing time t, the GR redshift between emission (e) and observation (o) is

$$(1+z)_{\rm GR} = \sqrt{\frac{-g_{tt}(x_o)}{-g_{tt}(x_e)}}\,, \tag{7}$$

a standard textbook result [1]. In our framework the physical lapse is rescaled by $A(\vartheta)$:

$$g_{tt} \;\to\; A(\vartheta)^2\, g_{tt}. \tag{8}$$

Therefore

$$1+z \;=\; \frac{\nu_e}{\nu_o} = \frac{A[\vartheta(x_o)]}{A[\vartheta(x_e)]}\sqrt{\frac{-g_{tt}(x_o)}{-g_{tt}(x_e)}}. \tag{9}$$

2.2 Schwarzschild specialization

For $ds^2 = -\big(1-r_s/r\big)\,dt^2 + \big(1-r_s/r\big)^{-1}dr^2 + r^2 d\Omega^2$,

$$1+z \;=\; \frac{A[\vartheta(r_o)]}{A[\vartheta(r_e)]}\sqrt{\frac{1-\frac{r_s}{r_o}}{1-\frac{r_s}{r_e}}}. \tag{10}$$

2.3 Weak-field expansion and null tests

With $-g_{tt} \simeq 1 + 2\Phi$ (Newtonian potential, $|\Phi| \ll 1$),

$$\Delta\ln\frac{\nu_o}{\nu_e} \;=\; \underbrace{\Delta\ln A}_{\text{new}} \;+\; \underbrace{\Delta\Phi}_{\text{GR}} \;+\; \mathcal{O}(\Phi^2)\,. \tag{11}$$

Given a fractional sensitivity σ_y over baseline L,

$$|\Delta\vartheta| \;\lesssim\; \frac{\sigma_y}{|g_\vartheta(\bar\vartheta)|}, \qquad |\nabla\vartheta| \;\lesssim\; \frac{\sigma_y/L}{|g_\vartheta(\bar\vartheta)|}. \tag{12}$$

Vertical comparisons use geodesy or local gravimetry to subtract $\Delta\Phi$, while fiber-linked or co-located clocks exploit common-mode rejection to isolate $\Delta\ln A$ [2–8].

2.4 Comments on κ and regularity

If $\kappa = 0$, $A(\vartheta) = \cos\vartheta$ can be arbitrarily small as $\vartheta \to \pi/2$ (but never zero by Axiom 3). Choosing $\kappa > 0$ keeps $A(\vartheta) \geq \sqrt{\kappa}\,\sin\vartheta$, avoiding near-vanishing lapse factors.

Illustration (Prediction 1). See Fig. 2: synthetic regression and GR–subtracted residuals visualize the $\Delta \ln A$ channel and the bounds of Eq. (12).

3 Open quantum dynamics: GKSL structure from the axioms (Note S3)

3.1 From pulsed projection to GKSL

Axiomatically, each pulse contributes a reversible increment along τ_r and an irreversible increment along τ_i. For a coarse-grained time step Δt that spans many pulses, linearity and complete positivity of reduced dynamics (Born–Markov–secular assumptions when appropriate) give a GKSL generator [9–11]:

$$\dot{\rho}_t = -\,i\,T_r[H,\rho_t] + T_i\,\mathcal{D}_\beta(\rho_t), \qquad T_r^2 + T_i^2 = 1, \tag{13}$$

with quantum detailed balance

$$\mathcal{D}_\beta(\rho) = \sum_\omega \gamma_\omega \Big(L_\omega \rho L_\omega^\dagger - \tfrac{1}{2}\{L_\omega^\dagger L_\omega, \rho\} \Big), \quad \gamma_{-\omega} = e^{-\beta\omega}\gamma_{+\omega}. \tag{14}$$

Axiom 3 enforces $T_i > 0$, hence irreversibility is *never* exactly switched off.

3.2 TLS example and the intrinsic floor

For a two-level system (TLS) with splitting Ω,

$$\Gamma_2^{\mathrm{obs}} = T_i\,\Gamma_2^{\mathrm{vac}} + \Gamma_2^{\mathrm{env}}, \qquad \Rightarrow \qquad \Gamma_2^{\mathrm{min}} \;\geq\; T_i\,\Gamma_2^{\mathrm{vac}}. \tag{15}$$

3.3 Bounding T_i in practice

Measure Γ_2 as a function of a control parameter that scales bath occupation/spectral density (e.g., temperature, engineered reservoir strength, readout power), fit Γ_2^{env}, and extrapolate to $\Gamma_2^{\mathrm{env}} \to 0$. With an independently calibrated Γ_2^{vac}, obtain

$$T_i \;\leq\; \frac{\Gamma_2^{\mathrm{min}}}{\Gamma_2^{\mathrm{vac}}} \quad (95\%\ \text{C.L.}). \tag{16}$$

Illustration (Prediction 2). See Fig. 3: regressions and bootstrap summaries quantify the intercept $T_i\Gamma_2^{\mathrm{vac}}$ and the bound in Eq. (16).

3.4 Thermodynamic consistency

Spohn's inequality implies monotonic decay of relative entropy and non-equilibrium free energy with a rate proportional to T_i [11, 12]:

$$\frac{d}{dt} D(\rho_t \| \rho_\beta) = -\,T_i\,\sigma(\rho_t) \leq 0, \qquad \frac{d}{dt} F(\rho_t) = -\,\frac{T_i}{\beta}\,\sigma(\rho_t) \leq 0. \tag{17}$$

4 Horizon thermality and analogue tests (Note S4)

4.1 Euclidean regularity

Near a static Killing horizon with surface gravity κ_{sg}, Euclidean time must be periodic with period $\beta_{\mathrm{proper}} = 2\pi/\kappa_{\mathrm{sg}}$ [13, 14]. The proper-time increment relates to the laboratory time as $d\tau_{\mathrm{proper}} = A(\vartheta)\,dt_r$, so

$$T_\infty = \frac{A(\vartheta_\infty)}{A(\vartheta_{\mathrm{hor}})}\,\frac{\kappa_{\mathrm{sg}}}{2\pi}. \tag{18}$$

GR is recovered when ϑ is constant.

4.2 Analogue platforms and ratio tests

Water tanks, fiber optics, and BEC horizons probe Hawking kinematics and correlations [15–21]. To test (18), compare otherwise identical runs a, b with controlled changes that co-vary with ϑ:

$$\frac{T_\infty^{(a)}}{T_\infty^{(b)}} = \frac{A(\vartheta_\infty^{(a)})/A(\vartheta_{\rm hor}^{(a)})}{A(\vartheta_\infty^{(b)})/A(\vartheta_{\rm hor}^{(b)})}. \tag{19}$$

5 Cosmological background and perturbations (Note S5)

5.1 Effective action and equations

Adopt a time-only disformal coupling for matter:

$$g_{\mu\nu}^{\rm eff} = g_{\mu\nu} + \big(A(\vartheta)^2 - 1\big) u_\mu u_\nu, \tag{20}$$

with u_μ a unit timelike one-form (e.g., ADM normal). The total action reads

$$S = \frac{M_{\rm Pl}^2}{2}\int d^4x\sqrt{-g}\,R + \int d^4x\sqrt{-g}\left[\frac{M_\vartheta^2}{2}\,\partial_\mu\vartheta\,\partial^\mu\vartheta - V(\vartheta)\right] + S_{\rm m}[\Psi, g^{\rm eff}(\vartheta)]\,. \tag{21}$$

Varying ϑ yields

$$M_\vartheta^2\,\Box\vartheta - V'(\vartheta) = A(\vartheta)A'(\vartheta)\,T^{\mu\nu}u_\mu u_\nu. \tag{22}$$

5.2 FRW background

In FRW, with $d\tau = A(\bar\vartheta)\,d\tau_r$, the standard scalar–field cosmology follows:

$$\rho_\vartheta = \tfrac{M_\vartheta^2}{2}\dot{\bar\vartheta}^2 + V(\bar\vartheta), \quad p_\vartheta = \tfrac{M_\vartheta^2}{2}\dot{\bar\vartheta}^2 - V(\bar\vartheta), \quad \ddot{\bar\vartheta} + 3H\dot{\bar\vartheta} + \frac{1}{M_\vartheta^2}V'(\bar\vartheta) = \frac{1}{M_\vartheta^2}AA'\,\rho_{\rm tot}. \tag{23}$$

Equation-of-state:

$$w_\vartheta = \frac{p_\vartheta}{\rho_\vartheta} = \frac{\frac{M_\vartheta^2}{2}\dot{\bar\vartheta}^2 - V(\bar\vartheta)}{\frac{M_\vartheta^2}{2}\dot{\bar\vartheta}^2 + V(\bar\vartheta)}. \tag{24}$$

5.3 Linear perturbations and forces

Fluctuations obey

$$\delta\vartheta: \quad \big(\Box - m_{\rm eff}^2\big)\delta\vartheta = \frac{1}{M_\vartheta^2}AA'\,\delta\rho, \tag{25}$$

with $m_{\rm eff}^2 = V''(\bar\vartheta) - \partial_{\bar\vartheta}(AA')\,\rho/M_\vartheta^2$. A fifth-force correction $\propto g_\vartheta^2/M_\vartheta^2$ is Yukawa-suppressed for $m_{\rm eff}r \gg 1$.

Illustration (Prediction 5). Figure 4 shows $H(z)/H_{\Lambda\rm CDM}(z)$ from the FRW integration (left, with a zoomed inset) and the corresponding $w_\vartheta(z)$ (right) for representative (κ, λ), illustrating the background drag from AA' in Eq. (22).

6 Time-direction tomography and correlated noise (Note S6)

6.1 Linear response of observables

Small fluctuations $\delta\vartheta$ modulate frequencies and rates via

$$\frac{\delta\omega}{\omega} = -\,g_\vartheta(\bar\vartheta)\,\delta\vartheta, \qquad \frac{\delta\Gamma}{\Gamma} = \cot\bar\vartheta\,\delta\vartheta. \tag{26}$$

6.2 Network model and cross spectra

For N sensors (clocks and/or qubits) at locations $\mathbf{x}_i$,

$$y_i(t) = c_i\,\delta\vartheta(\mathbf{x}_i, t) + n_i(t), \qquad c_i \in \{-g_\vartheta(\bar{\vartheta}_i),\, \cot\bar{\vartheta}_i\}. \tag{27}$$

Cross-power spectra satisfy, for $i \neq j$,

$$S_{ij}(f) \simeq c_i c_j\, S_\vartheta(f) + \delta_{ij} S_{n_i}(f). \tag{28}$$

A maximum-likelihood or Bayesian fit to $\{S_{ij}\}$ across frequencies reconstructs $S_\vartheta(f)$ and tests spatial correlations. Co-located heterogeneous pairs (clock+qubit) over-constrain the sign/magnitude of c_i. Clock-network correlation analyses can follow pipelines developed for ultralight-field searches [5, 6, 22, 23].

Illustration (Prediction 6). Figure 5 displays (left) the recovery of the common-field PSD $S_\vartheta(f)$ from cross spectra versus the injected truth, and (right) a band-averaged magnitude-squared coherence matrix across sensors, both derived from the linear responses in Eq. (26) and the network model in Eq. (27). Figure 6 provides complementary network-level views.

7 Parameterizations, priors, and identifiability (Note S7)

Baseline parameters. Today's background $\bar{\vartheta}_0 \in (0, \pi/2)$; coupling balance $\kappa \geq 0$; kinetic scale M_ϑ; potential $V(\vartheta)$ (e.g., quadratic near minimum, cosine, or slow-roll plateau).

Degeneracies. Redshift tests constrain $g_\vartheta(\bar{\vartheta})$ gradients, while decoherence floors constrain $T_i = \sin\bar{\vartheta}$; together they bound complementary functions of $\bar{\vartheta}$. Cosmology probes a mixture of (M_ϑ, V) with background drag $AA'\rho$.

Priors. Positivity ($M_\vartheta^2 > 0$, $A > 0$), endpoint exclusion ($\bar{\vartheta} \notin \{0, \pi/2\}$), and mildness of g_ϑ today (to satisfy local tests). For $V(\vartheta)$ use minimally structured priors.

8 Statistical procedures and uncertainty (Note S8)

8.1 Clock redshift bounds

Use (11) and (12) with Allan deviations mapped to σ_y at the averaging time of the comparison [3]. For vertical comparisons, subtract $\Delta\Phi$ from geopotential models or local gravimetry. Report bounds on $|\Delta\vartheta|$ and $|\nabla\vartheta|$ at 68/95% C.L.

8.2 Decoherence floor

Fit Γ_2 vs. control parameter using heteroscedastic weighted least squares; perform leave-one-out cross-validation to guard against model bias in Γ_2^{env}. Propagate fit covariances to the ratio bound (16). Engineered-reservoir strategies follow Myatt et al. [24].

8.3 Network tomography

Estimate cross-spectra with Welch averaging; use a multivariate Gaussian likelihood in frequency space for $\{S_{ij}(f)\}$. Nuisance terms: sensor-specific noise floors, clock drifts, and transfer-function calibration [5, 6, 25, 26].

9 Consistency checks and absence of pathologies (Note S9)

No ghosts. The scalar ϑ is canonical with positive kinetic term $M_\vartheta^2 > 0$.

GR limit. Constant ϑ reduces to pure GR after redefining time by $t_{\rm phys} = A(\vartheta_0)\, t$ [1].

Thermodynamic consistency. QDB ensures KMS stationarity and Spohn's inequality; $T_i > 0$ scales rates but does not violate the second law [11, 12, 27, 28].

Laboratory consistency. For $\kappa > 0$ and ϑ bounded away from endpoints, $A(\vartheta)$ is regular and monotone between the axes; no singular lapse factors occur.

10 Extended notes and worked examples (Note S10)

10.1 Worked weak-field null test

Two identical clocks at heights separated by Δh give

$$\Delta \ln \frac{\nu_o}{\nu_e} \simeq \Delta\Phi + g_\vartheta(\bar\vartheta)\, \Delta\vartheta, \tag{29}$$

with $\Delta\Phi \simeq g\, \Delta h/c^2$. Using $\sigma_y = 1 \times 10^{-18}$ at $10^3\,$s and $\Delta h = 0.5\,$m,

$$|\nabla\vartheta| \;\lesssim\; \frac{2 \times 10^{-18}\,\mathrm{m}^{-1}}{|g_\vartheta(\bar\vartheta)|}. \tag{30}$$

See [2, 3, 29–31].

10.2 TLS spectroscopy protocol

Tune the bath temperature and engineered-reservoir strength to collapse $\Gamma_2^{\rm env} \to 0$. Measure $\Gamma_2^{\rm min}$ and compare to $\Gamma_2^{\rm vac}$ inferred from geometry/couplings (or from extrapolated $T \to 0$ scaling). Quote T_i from (16). See [24, 32, 33].

10.3 Analogue horizon ratio test

In BEC, vary the flow profile to change the near-horizon $A(\vartheta_{\rm hor})$ while keeping $\kappa_{\rm sg}$ fixed (within calibration). Measure T_∞ via spectral fits and pair correlations in two settings (a, b); test the predicted ratio. See [15–21].

11 Distinctiveness and relation to other frameworks (Note S11)

This Note expands the "Distinctiveness" paragraph in the Main by placing the present proposal alongside several well–known ideas. In brief: the time-direction field introduced here is *internal* (lives in a two–dimensional auxiliary plane with coordinates (τ_r, τ_i)), has fixed norm $T_r^2 + T_i^2 = 1$, and its *direction* $\vartheta(x)$ simultaneously (i) rescales physical lapse factors in gravity via $A(\vartheta)$ and (ii) weights coherent versus dissipative evolution in open quantum dynamics via the GKSL/KMS structures.

A. Versus Einstein–Æther and Hořava gravity

EA and HL modify spacetime via a new vector/foliation; here $\vec{T}$ is internal and couples to intervals only through $A(\vartheta)$ while also weighting GKSL dynamics [9–11, 27, 28, 34, 35].

B. Versus the Thermal Time Hypothesis

TTH ties flow to modular automorphisms without altering metric intervals [36]; our $A(\vartheta)$ rescales intervals and yields falsifiable redshift/decoherence predictions.

C. Versus two-time physics

2T adds a macroscopic time dimension [37, 38]; here no extra spacetime dimension appears—the "second direction" is internal.

D. Versus discrete-time ideas

Chronons and causal sets implement discreteness in spacetime [39, 40]; here discreteness resides (if at all) in the pulses of an internal unit vector, with a smooth GKSL/GR limit after coarse graining.

E. Summary table

Framework	New spacetime d.o.f.?	Modifies metric intervals?	Couples to GKSL/KMS?
Einstein–Æther [34]	Yes (u^μ)	Yes	No
Hořava gravity [35]	Yes (foliation)	Yes	No
Thermal Time Hypothesis [36]	No	No	Via modular theory
Two-time physics [37, 38]	Yes (extra time)	Yes	No
Chronon [39]	No (discrete t)	Yes	No
Causal set [40]	Yes (atoms)	Yes	No
This work	**No (internal $\vec{T}$)**	**Yes (via $A(\vartheta)$)**	**Yes (weights T_r, T_i)**

Table 1: Contrasts between the present internal time-direction framework and related ideas.

Figures

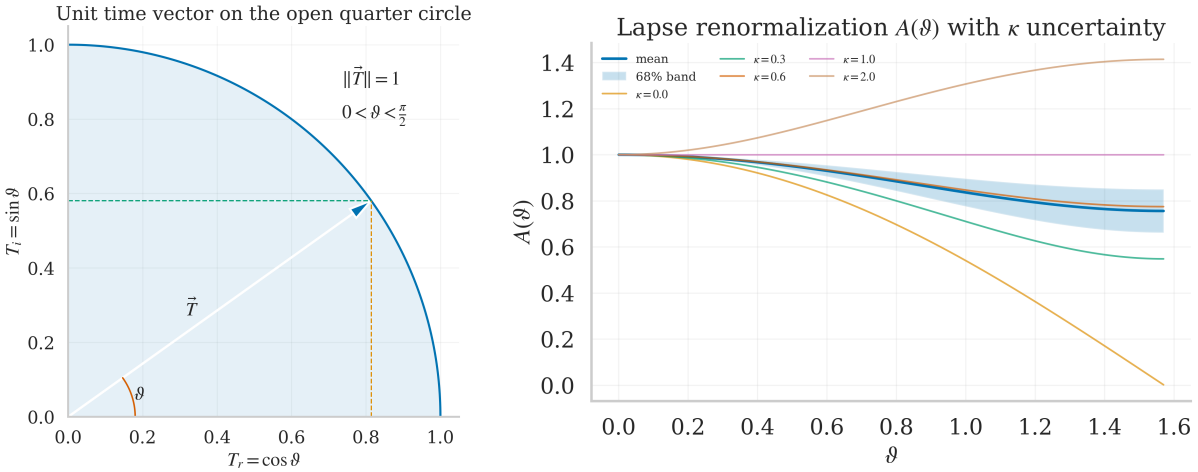

Figure 1: **Theory primitives (Notes S1–S2; supports Predictions 1–6). (left)** Geometry of the internal unit-time vector $\vec{T} = (T_r, T_i) = (\cos\vartheta, \sin\vartheta)$ restricted to the open quarter circle $0 < \vartheta < \pi/2$ (Axioms 1–2). This encodes the irreducible blend of coherent (T_r) and dissipative (T_i) directions that later weights GKSL dynamics (Note S3). **(right)** Lapse renormalization $A(\vartheta) = \sqrt{\cos^2\vartheta + \kappa\sin^2\vartheta}$ with a 68% Monte-Carlo ribbon over κ. The special case $\kappa = 1$ yields $A \equiv 1$ (pure-GR normalization); $\kappa \neq 1$ tilts the balance and induces the logarithmic response $g_\vartheta = \partial_\vartheta \ln A$ used in the redshift renormalization (Note S2), the linear responses of observables (Note S6), and the cosmological background drag (Note S5).

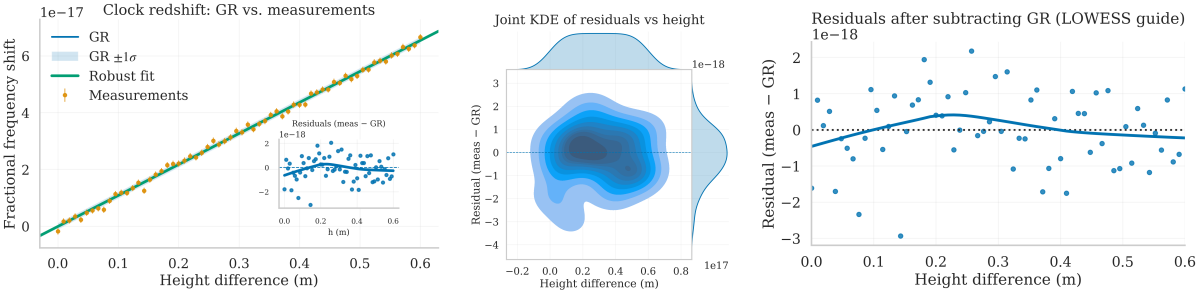

Figure 2: **Prediction 1 — Clock redshift renormalization (Note S2).** Synthetic weak-field comparisons demonstrate how $\Delta\ln A$ appears as a residual after GR subtraction in Eq. (11). **(left)** Weighted regression linking the measured fractional frequency shift to the modeled GR contribution plus a free $\Delta\ln A$ term; unity slope corresponds to the GR mapping, while the fitted offset captures the putative $A(\vartheta)$ contribution across baselines. **(middle)** Joint credibility for the regression parameters (e.g. slope and offset), highlighting the constraint on $\Delta\ln A$ that maps to $|\Delta\vartheta| \lesssim \sigma_y/|g_\vartheta(\bar{\vartheta})|$ via Eq. (12). **(right)** GR-subtracted residuals versus control (height or potential), isolating the additional channel $\Delta\ln A$; bands show $\pm1\sigma$ about the best fit. Together these panels visualize the pipeline used for vertical/fiber-linked null tests in Note S2.

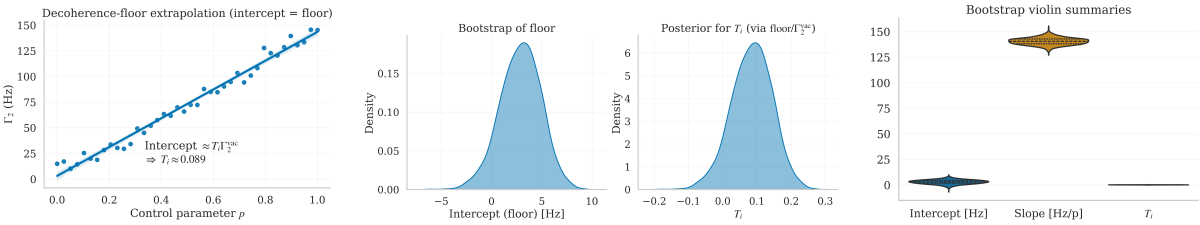

Figure 3: **Prediction 2 — Irreducible decoherence floor (Note S3).** Open-system fits recover the intrinsic limit implied by Axiom 3 through Eq. (15). **(left)** Representative regression of the measured dephasing rate Γ_2 versus a control that tunes the environmental channel (temperature, engineered reservoir strength, readout power), with extrapolation to $\Gamma_2^{\rm env} \to 0$; the intercept estimates $T_i\,\Gamma_2^{\rm vac}$. **(middle)** Nonparametric uncertainty from bootstrap resampling of the full regression procedure (point clouds/paths show many refits), quantifying robustness against heteroscedastic noise and model choice. **(right)** Violin/summary of the resulting intercept distribution, reported as a bound on T_i through Eq. (16). This implements the practical protocol described in Note S3 and the statistics workflow in Note S8.

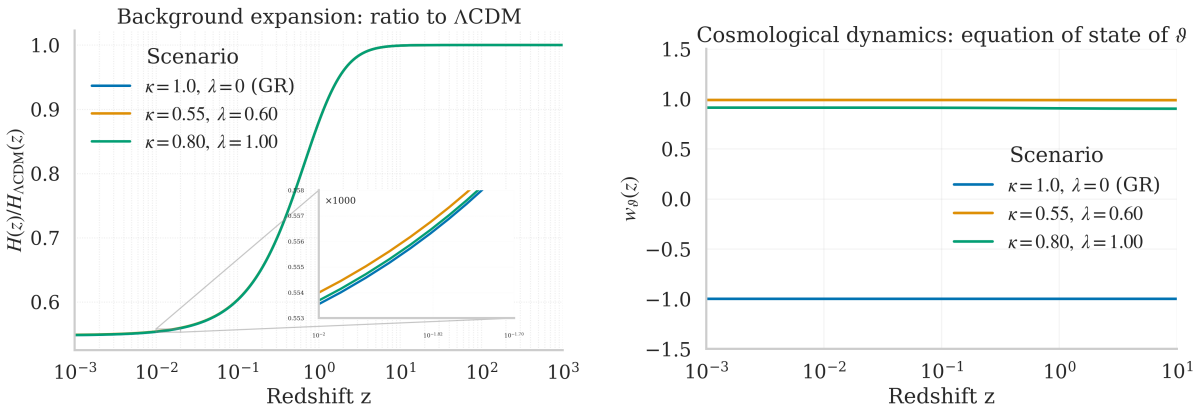

Figure 4: **Prediction 5 — Cosmology (background; Note S5). (left)** background expansion ratio $H(z)/H_{\Lambda\mathrm{CDM}}(z)$ obtained from the FRW system in Note 5, with an inset magnifying $z \in [10^{-2}, 10^{-1}]$ to expose the $\sim 10^{-3}$-level separations among scenarios (set by the $A(\vartheta)$ drag term in Eq. (22) and the FRW equations). **(right)** the corresponding equation of state $w_\vartheta(z)$ from the same runs. These curves illustrate small, structured departures that precision BAO/SN datasets could test.

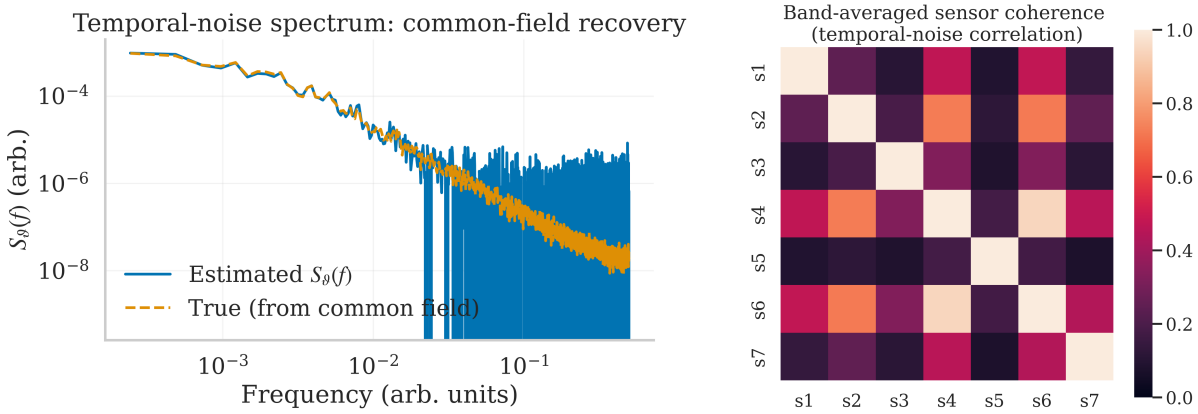

Figure 5: **Prediction 6 — Correlated temporal-noise signatures (Note S6). (left)** recovery of the common-field PSD $S_\vartheta(f)$ (solid) from cross spectra of a heterogeneous sensor network using Eq. (27); the dashed curve is the injected truth. **(right)** band-averaged magnitude-squared coherence matrix across sensors showing the expected correlation pattern from a shared $\delta\vartheta(t)$ driver; see the linear responses in Eq. (26).

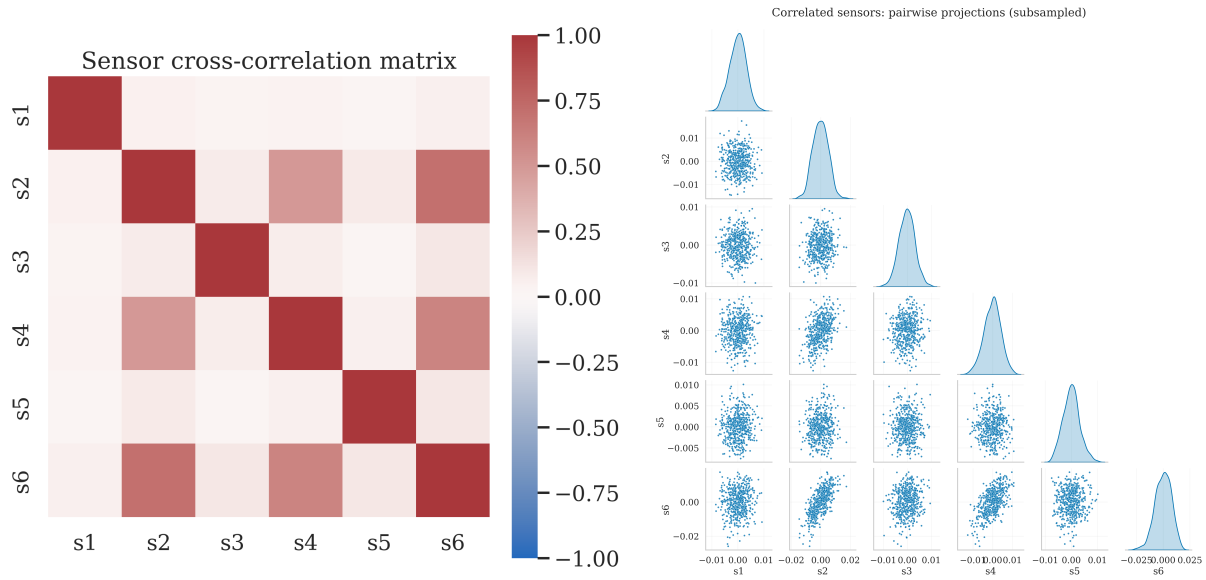

Figure 6: **Network views for correlated time-direction noise (Note S6; supports Prediction 6). (left)** Band-averaged magnitude-squared coherence between all sensor pairs, computed from Welch-averaged cross spectra over a fixed frequency window (Note S6). The unity diagonal reflects autospectra; off-diagonal contrast encodes the common $\delta\vartheta(t)$ drive through $S_{ij} \simeq c_i c_j S_\vartheta$ with $c_i \in \{-g_\vartheta(\bar{\vartheta}_i), \cot\bar{\vartheta}_i\}$ (Eqs. (26)–(27)). **(right)** Pairwise projections of (demeaned, standardized) time-series segments for selected channels, illustrating correlated structure and relative signs consistent with the $c_i c_j$ pattern. These diagnostics complement Fig. 5, where the same cross-spectral information is used to recover the common-field PSD $S_\vartheta(f)$.

Inventory of Supplementary Materials

- **Supplementary Notes:** S1–S11 (axioms/definitions; redshift renormalization; GKSL structure and intrinsic floor; horizon thermality; cosmology; network tomography; parameterizations and priors; statistics; consistency checks; worked examples; distinctiveness vs. related frameworks).
- **Supplementary Figures:** Six synthetic figures (S1–S6). Main Fig. 1 (theory primitives) corresponds to S1; Main Fig. 2 (four near-term tests) assembles panels drawn from S2 (redshift regression), S3 (decoherence regression), S5 ($H/H_{\Lambda\mathrm{CDM}}$ with inset), and S6 (common-field PSD recovery).

  Fig. S1. Theory primitives (Notes S1–S2; supports all predictions).

  Fig. S2. **Prediction 1** (Note S2): redshift regression and residuals.

  Fig. S3. **Prediction 2** (Note S3): decoherence-floor regression and bootstraps.

  Fig. S4. **Prediction 5** (Note S5): $H/H_{\Lambda\mathrm{CDM}}$ with zoom inset and $w_\vartheta(z)$.

  Fig. S5. **Prediction 6** (Note S6): common-field PSD recovery and sensor coherence.

  Fig. S6. Network views for **Prediction 6** (Note S6): correlation heatmap and pairplot.

- **Supplementary Tables:** one in this SI (Table 1, "Distinctiveness and relation to other frameworks" in Note S11). There are no tables in the Main.
- **Supplementary Software:** Python scripts for synthetic-data generation and figure production (fixed RNG seeds). To be deposited upon submission and archived upon publication.

Data and code availability

All calculations are analytical. Synthetic-data generators and analysis scripts for the redshift null tests, decoherence-floor fits, horizon ratio tests, cosmology backgrounds, and network tomography

are available in the `data` directory and will be deposited upon submission and archived upon publication.

References

[1] R. M. Wald. *General Relativity*. University of Chicago Press, 1984. DOI: 10.7208/chicago/9780226870373.001.0001.

[2] C. W. Chou et al. "Optical Clocks and Relativity." In: *Science* 329.5999 (2010), pp. 1630–1633. DOI: 10.1126/science.1192720.

[3] A. D. Ludlow et al. "Optical atomic clocks." In: *Reviews of Modern Physics* 87.2 (2015), pp. 637–701. DOI: 10.1103/RevModPhys.87.637.

[4] T. Takano et al. "Geopotential measurements with synchronously linked optical lattice clocks." In: *Nature Photonics* 10 (2016), pp. 662–666. DOI: 10.1038/nphoton.2016.159.

[5] C. Lisdat et al. "A clock network for geodesy and fundamental science." In: *Nature Communications* 7 (2016), p. 12443. DOI: 10.1038/ncomms12443.

[6] BACON Collaboration. "Frequency ratio measurements at 18-digit accuracy using an optical clock network." In: *Nature* 591 (2021), pp. 564–569. DOI: 10.1038/s41586-021-03253-4.

[7] P. Delva et al. "Gravitational Redshift Test Using Eccentric Galileo Satellites." In: *Physical Review Letters* 121 (2018), p. 231101. DOI: 10.1103/PhysRevLett.121.231101.

[8] S. Herrmann et al. "Test of the gravitational redshift with Galileo satellites in an eccentric orbit." In: *Physical Review Letters* 121 (2018), p. 231102. DOI: 10.1103/PhysRevLett.121.231102.

[9] V. Gorini, A. Kossakowski, and E. C. G. Sudarshan. "Completely Positive Dynamical Semigroups of N-Level Systems." In: *Journal of Mathematical Physics* 17.5 (1976), pp. 821–825. DOI: 10.1063/1.522979.

[10] G. Lindblad. "On the Generators of Quantum Dynamical Semigroups." In: *Communications in Mathematical Physics* 48.2 (1976), pp. 119–130. DOI: 10.1007/BF01608499.

[11] H.-P. Breuer and F. Petruccione. *The Theory of Open Quantum Systems*. Oxford University Press, 2002. DOI: 10.1093/acprof:oso/9780199213900.001.0001.

[12] H. Spohn. "Entropy Production for Quantum Dynamical Semigroups." In: *Journal of Mathematical Physics* 19.5 (1978), pp. 1227–1230. DOI: 10.1063/1.523789.

[13] G. W. Gibbons and S. W. Hawking. "Action Integrals and Partition Functions in Quantum Gravity." In: *Physical Review D* 15.10 (1977), pp. 2752–2756. DOI: 10.1103/PhysRevD.15.2752.

[14] S. W. Hawking. "Particle Creation by Black Holes." In: *Communications in Mathematical Physics* 43.3 (1975), pp. 199–220. DOI: 10.1007/BF02345020.

[15] W. G. Unruh. "Experimental black-hole evaporation?" In: *Physical Review Letters* 46.21 (1981), pp. 1351–1353. DOI: 10.1103/PhysRevLett.46.1351.

[16] C. Barceló, S. Liberati, and M. Visser. "Analogue gravity." In: *Living Reviews in Relativity* 14.3 (2011). DOI: 10.12942/lrr-2011-3.

[17] T. G. Philbin et al. "Fiber-Optical Analog of the Event Horizon." In: *Science* 319.5868 (2008), pp. 1367–1370. DOI: 10.1126/science.1153625.

[18] S. Weinfurtner et al. "Measurement of Stimulated Hawking Emission in an Analogue System." In: *Physical Review Letters* 106 (2011), p. 021302. DOI: 10.1103/PhysRevLett.106.021302.

[19] L.-P. Euvé et al. "Observation of Noise Correlated by the Hawking Effect in a Water Tank." In: *Physical Review Letters* 117 (2016), p. 121301. DOI: 10.1103/PhysRevLett.117.121301.

[20] J. Drori et al. "Observation of Stimulated Hawking Radiation in an Optical Analogue." In: *Physical Review Letters* 122 (2019), p. 010404. DOI: 10.1103/PhysRevLett.122.010404.

[21] J. Steinhauer. "Observation of quantum Hawking radiation and its entanglement in an analogue black hole." In: *Nature Physics* 12 (2016), pp. 959–965. DOI: 10.1038/nphys3863.

[22] A. Derevianko and M. Pospelov. "Hunting for topological dark matter with atomic clocks." In: *Nature Physics* 10 (2014), pp. 933–936. DOI: 10.1038/nphys3137.

[23] P. Wcisło et al. "Experimental constraint on dark matter detection with optical atomic clocks." In: *Nature Astronomy* 1, 0009 (2017). DOI: 10.1038/s41550-016-0009.

[24] C. J. Myatt et al. "Decoherence of quantum superpositions through coupling to engineered reservoirs." In: *Nature* 403.6767 (2000), pp. 269–273. DOI: 10.1038/35002001.

[25] G. de Lange et al. "Universal Dynamical Decoupling of a Single Solid-State Spin from a Spin Bath." In: *Science* 330.6000 (2010), pp. 60–63. DOI: 10.1126/science.1192739.

[26] S. Kotler et al. "Single-ion quantum lock-in amplifier." In: *Nature* 473 (2011), pp. 61–65. DOI: 10.1038/nature10010.

[27] R. Kubo. "The fluctuation-dissipation theorem." In: *Reports on Progress in Physics* 29 (1966), pp. 255–284. DOI: 10.1088/0034-4885/29/1/306.

[28] P. C. Martin and J. Schwinger. "Theory of Many-Particle Systems. I." In: *Physical Review* 115.6 (1959), pp. 1342–1373. DOI: 10.1103/PhysRev.115.1342.

[29] T. Bothwell et al. "Resolving the gravitational redshift within a millimetre-scale atomic sample." In: *Nature* 602 (2022), pp. 420–424. DOI: 10.1038/s41586-021-04349-7.

[30] X. Zheng et al. "Differential clock comparisons with a multiplexed optical lattice clock." In: *Nature* 602 (2022), pp. 425–430. DOI: 10.1038/s41586-021-04344-y.

[31] X. Zheng et al. "A lab-based test of the gravitational redshift with a miniature clock network." In: *Nature Communications* 14 (2023), p. 4886. DOI: 10.1038/s41467-023-40629-8.

[32] A. J. Leggett. "Testing the limits of quantum mechanics: motivation, state of play, prospects." In: *Journal of Physics: Condensed Matter* 14.15 (2002), R415–R451. DOI: 10.1088/0953-8984/14/15/201.

[33] M. Kjaergaard et al. "Superconducting Qubits: Current State of Play." In: *Annual Review of Condensed Matter Physics* 11 (2020), pp. 369–395. DOI: 10.1146/annurev-conmatphys-031119-050605.

[34] T. Jacobson and D. Mattingly. "Gravity with a dynamical preferred frame." In: *Physical Review D* 64 (2001), p. 024028. DOI: 10.1103/PhysRevD.64.024028.

[35] D. Blas, O. Pujolàs, and S. Sibiryakov. "Models of nonrelativistic quantum gravity: The good, the bad, and the healthy." In: *Journal of High Energy Physics* 2011.4 (2011), p. 018. DOI: 10.1007/JHEP04(2011)018.

[36] A. Connes and C. Rovelli. "Von Neumann algebra automorphisms and time-thermodynamics relation in generally covariant quantum theories." In: *Classical and Quantum Gravity* 11.12 (1994), pp. 2899–2918. DOI: 10.1088/0264-9381/11/12/007.

[37] I. Bars. "Two-time physics in field theory." In: *Physical Review D* 62 (2000), p. 046007. DOI: 10.1103/PhysRevD.62.046007.

[38] I. Bars. "Survey of two-time physics." In: *Classical and Quantum Gravity* 18.16 (2001), pp. 3113–3130. DOI: 10.1088/0264-9381/18/16/303.

[39] P. Caldirola. "The introduction of the chronon in the electron theory and a charged lepton mass formula." In: *Il Nuovo Cimento B* 53.2 (1980), pp. 291–326. DOI: 10.1007/BF02750348.

[40] L. Bombelli et al. "Space-Time as a Causal Set." In: *Physical Review Letters* 59.5 (1987), pp. 521–524. DOI: 10.1103/PhysRevLett.59.521.